REVISTA MATÉRIA V.30
ISSN 1517-7076 articles e20250258, 2025

Fabrication characterization and mechanical properties of gradient triply periodic minimal surface structures via fused deposition modeling

Heng-Liang Fan[1,2], Abdullah Yassin[1]

[1]Universiti Malaysia Sarawak, Faculty of Engineering. Malaysia, 94300, Kota Samarahan, Sarawak, Malaysia.
[2]Bengbu University, School of Mechanical and Vehicle Engineering. Bengbu. 233030, Bengbu, Anhui, China.
e-mail: yabdulla@unimas.my, fhl209@126.com

ABSTRACT

Triply periodic minimal surface (TPMS) structures have gained significant interest due to their excellent mechanical characteristics and diverse range of applications across various fields. This study systematically designs and analyzes uniform and gradient porous structures based on Primitive and Gyroid TPMS geometries. The samples were fabricated using fused deposition modeling (FDM) with polylactic acid (PLA). Their morphologies were characterized via optical microscopy and micro-computed tomography (micro-CT), and quasi-static compression tests were performed under controlled conditions to evaluate their mechanical properties. The results demonstrated that the fabricated pore characteristics closely matched with the design parameters. For the uniform structures, yield strength decreased from 11.26 MPa at 30% porosity to 2.24 MPa at 50% porosity, and the elastic modulus decreased from 309.8 MPa to 167.1 MPa as porosity increased from 30% to 50%. At the same porosity, uniform structures exhibited higher yield strength than gradient structures. Additionally, an empirical equation derived from the Gibson-Ashby model was introduced to predict the compressive behavior of porous structures based on their relative density. These findings provide essential guidance for designing lightweight structures with enhanced mechanical properties, highlighting the potential of TPMS porous structures for advanced engineering applications.

Keywords: Triply periodic minimal surface; Fused deposition modeling; Gradient porous structure; Energy absorption.

1. INTRODUCTION

Porous structures offer numerous advantages, including reduced relative density, minimal weight, and a large specific surface area. These features enhance their mechanical strength, vibration damping efficiency, and energy absorption capacity [1]. These characteristics make them widely applicable in various fields, including mechanical engineering [2], aerospace [3], and medicine [4], among others [5]. These structures are particularly valued for their high specific surface area, which is advantageous in various thermal applications [6]. Recent advancements in TPMS structures have enabled the development of lightweight materials with superior mechanical properties and energy absorption capabilities. Studies have highlighted the role of computational modeling in optimizing the design of TPMS for various applications, including aerospace, biomedical, and energy storage systems. For instance, the computational design of TPMS geometries has been extensively explored for their potential in enhancing the structural integrity and energy absorption capacity of lattice materials [7]. Additionally, TPMS-based composites have been studied for their application in lightweight structural elements with enhanced performance in dynamic loading scenarios [8]. The flexibility of TPMS structures has also been exploited in the development of advanced thermal management and energy storage materials, where the interconnected pore networks provide enhanced heat transfer and energy storage capabilities [9]. Beyond mechanical applications, TPMS architectures are gaining traction in functional systems like energy storage. LESMANA *et al.* experimentally validated Gyroid-based reactors for hydrogen storage, highlighting the role of TPMS porosity in facilitating mass transport [10]. However, one of the primary challenges in their development lies in manufacturing porous structures with predictable volume fractions. This is further complicated by the limitations of traditional production techniques, which often struggle to create optimized internal architectures that meet the demands of specific applications.

Corresponding Author: Abdullah Yassin Received on 20/03/2025 Accepted on 21/07/2025

DOI: https://doi.org/10.1590/1517-7076-RMAT-2025-0258

Recent advancements in additive manufacturing (AM) techniques, such as selective laser sintering (SLS) [11], selective laser melting (SLM) [12], and fused deposition modeling (FDM) [13], have greatly improved the ability to produce porous structures with intricate and highly accurate geometries. These techniques allow for the preservation of intricate internal networks, which are essential for maintaining structural integrity and functionality. Additionally, recent studies have explored the specific functionalities of PLA-based materials in AM, demonstrating their versatile applications and promising performance in various sectors. For instance, Alizadeh-Osgouei et al highlighted the advancements in high-strength PLA-based scaffolds for tissue engineering applications [14]. ZHAO *et al.* [15] investigated the impact of PLA modifications on mechanical properties and degradation behavior to improve biomedical performance [15]. Furthermore, Li developed an analysis of PLA composites and their potential for industrial applications, particularly in manufacturing porous structures with enhanced properties [16]. Optimization of hybrid TPMS structures for multi-physics performance remains an active frontier. YE *et al.* [17] combined mechanical and thermal analysis of hybrid lattices, underscoring the interdependence of geometric parameters and functional properties [17]. Consequently, research aimed at improving the quality and performance of porous structures has gained significant attention. Al-Ketan *et al.* utilized selective laser melting to fabricate lamella-based 316L stainless steel powder structures from, investigating their mechanical properties and anisotropic behavior through a combination of experimental methods and finite element modeling [18]. Similarly, LI *et al.* [19] optimized body-centered cube (BCC) structure to develop face-centered cube (FCCZ) and face-centered cube with vertical support (FBCCZ) designs, achieving strength improvements of 18.77% and 18.43%, respectively, compared to BCC [19]. PARK *et al.* [20] developed a comprehensive database of lattice structure attributes and proposed an optimized design approach to select compression-dominant structures, correlating mechanical properties with cell type, lattice topology, relative density, and cell arrangement [20]. Despite certain limitations in mechanical strength and energy absorption capabilities, these porous structures hold significant potential for specific engineering applications, particularly where lightweight and customizable designs are required. Beyond mechanical and biomedical applications, TPMS geometries have demonstrated significant potential in thermal management and energy-related systems. For instance, TPMS-based heat exchangers and flow-through channels can greatly enhance convective heat transfer in compact thermal devices [21]. Likewise, the high specific surface area and interconnected porosity of TPMS architectures make them attractive candidates for phase-change and sorption-based energy storage media, where controlled pore networks improve mass/heat transport and storage density. These features allow TPMS structures to operate as effective thermal spreaders, battery-cooling substrates, and high-performance adsorbents in advanced energy systems [22].

The study of porous materials and their mechanical properties is deeply rooted in the foundational work of Gibson and Ashby. Their work, particularly on the relationship between relative density and mechanical properties, has been essential in understanding how porosity affects the strength, stiffness, and energy absorption capacity of these structures [23]. This framework has influenced the design and optimization of many porous structures, including TPMS lattices, by providing predictive models for how changes in porosity can alter their behavior under various loading conditions. Recent studies have increasingly focused on TPMS porous structures, a type of lattice structure with unique characteristics and a wide range of potential applications [24]. These structures offer significant advantages, including enhanced mechanical properties, a lightweight nature, and high energy absorption capacity, making them suitable for various engineering fields. JIA *et al.* [25] fabricated P-TPMS structures based on SLS and showed that the Primitive TPMS design achieved superior elastic modulus and compressive strength compared to alternative configurations [25]. AL-KETAN *et al.* [26] utilized additive manufacturing (AM) processes to fabricate hierarchical TPMS structures using AISi10Mg alloy, tailoring its mechanical properties for targeted applications [26]. Similarly, LIANG *et al.* [27] fabricated P-TPMS and G-TPMS structures with relative densities ranging from 25% to 42% and cell sizes between 0.2 and 0.4 mm [27]. LIANG *et al.* [27] produced Primitive (P) and Gyroid (G) structures with porosity ranging from 25% to 42% and cell dimensions varying between 0.2 and 0.4 mm. PENG *et al.* [28] designed sandwich IWP structures using additive manufacturing technology, evaluating their mechanical properties through compression testing [28]. CAO *et al.* [29] explored the effects of additive manufacturing defects on the mechanical properties of TPMS structures, finding that slice thickness significantly impacted the overall performance [29]. Additionally, PENG *et al.* [30] investigated the compressive properties and deformation behavior of G-TPMS structures produced using FDM and carbon fiber-reinforced polymer composites [30]. HU *et al.* [31] studied the damage evolution and internal feature failure processes of G-TPMS structures, while highlighting that the periodicity of these structures allows for more predictable stress behavior using computer-aided design models [31]. Recent studies on gradient TPMS designs have extended to dynamic loading scenarios. For instance, LU *et al.* [32] investigated multidimensional gradient Gyroid structures under static and dynamic loads, demonstrating superior energy absorption via layer-wise collapse mechanisms [32]. HIRMUKHE *et al.* [33] uses finite element

analysis to investigate the deformation and failure mechanisms of nanoscale hexagonal cellular structures made from metallic glasses, highlighting their mechanical behavior and failure modes under various loading conditions [33]. Based on the existing literature, this study aims to systematically investigate the influence of porosity on compressive properties. However, despite previous studies, the precise relationship between variations in porosity, cell types, and mechanical properties remains insufficiently explored. To address these gaps, this study employs experimental validation and computational modeling to evaluate the interplay of these factors, providing a comprehensive understanding of TPMS structure design for advanced applications.

Both Primitive and Gyroid TPMS are widely studied and used in additive manufacturing due to their highly interconnected porosity, which allows for improved mechanical properties such as strength, stiffness, and energy absorption. These structures are well-known for their versatility and have been the focus of numerous studies, making them ideal candidates for comparison and analysis. The Primitive TPMS is known for its relatively simpler geometry, which typically provides better stiffness but lower energy absorption under compression compared to the more complex Gyroid TPMS. Gyroid, on the other hand, has a more intricate geometry that can lead to better energy absorption and more efficient load distribution, making it an excellent candidate for applications where shock absorption is critical.

In this study, Primitive (P) and Gyroid (G) TPMS porous structures were designed and fabricated via fused deposition modeling (FDM). The morphologies of the samples were characterized via optical microscopy and micro-computed tomography (micro-CT). Quasi-static compression tests were conducted to evaluate the mechanical properties. Additionally, this study aimed to investigate the influence of critical structural parameters, including porosity and unit cell geometry, on compressive strength and energy absorption capabilities. The results offer important insights that deepen the understanding of their mechanical properties and expand their potential use in various engineering applications. The findings provide important insights that deepen the understanding of their mechanical properties and expand their potential applications in various engineering field.

2. STRUCTURAL DESIGN AND METHODS

2.1. TPMS surfaces

A TPMS is defined by its unique property that at every point on its surface, it has zero mean curvature. One widely used modeling method involves approximating the TPMS geometry through an implicit sinusoidal periodic function, as represented by the following equation [34]:

$$\varphi_{(r)} = \sum_1^k A_k cos[2\pi(h_k r)\delta_k + P_k] = T \tag{1}$$

Where r is the position vector in Euclidean space, h_k is the kth lattice vector in inverse space, A_k is the amplitude factor, k is the wavelength of the cycle, p_k is the phase, and T is the threshold.

An ideal structural model can be obtained by establishing different types of implicit expressions, thus enabling the acquisition of a more accurate TPMS structural model. To obtain adjustable parameters for models with different porosities, the Primitive (P) and Gyroid (G) TPMS functions with adjustable parameters can be described [35]:

$$\varphi_P = \cos\left(\frac{2\pi}{L}x\right) + \cos\left(\frac{2\pi}{L}y\right) + \cos\left(\frac{2\pi}{L}z\right) \tag{2}$$

$$\varphi_G = \cos\left(\frac{2\pi}{L}x\right)\sin\left(\frac{2\pi}{L}y\right) + \cos\left(\frac{2\pi}{L}y\right)\sin\left(\frac{2\pi}{L}z\right) + \cos\left(\frac{2\pi}{L}z\right)\sin\left(\frac{2\pi}{L}x\right) \tag{3}$$

Where L is the unit-cell size. x, y, and z represent spatial coordinates.T_P (T_G) is the level-set parameter used to control the porosity of the TPMS structures. The cell dimension and the porosity can be modified by adjusting the parameters L and T. To generate cells with the desired porosity, a mathematical model of the parameter T with porosity ρ* was constructed. Figure 1 illustrates the correlation between T and ρ∗ for both uniform P and G structures.

Primitive TPMS offers high stiffness and stability, making it ideal for applications requiring strength and load-bearing capacity, such as in structural components. While more complex, the Gyroid structure is

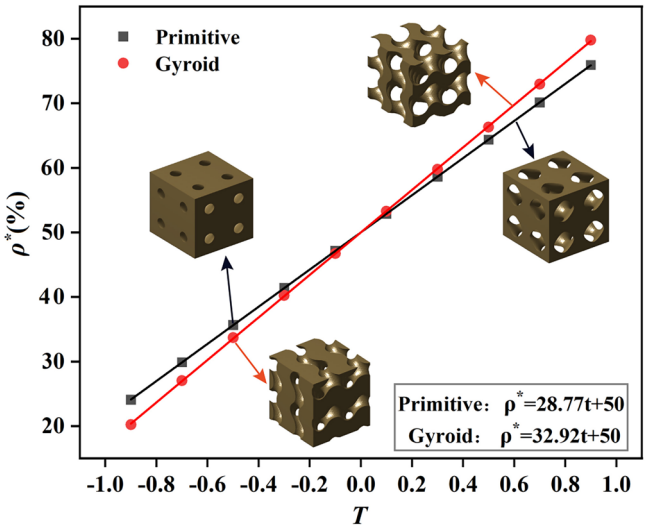

Figure 1: Relationship between *T* and ρ* for P and G structures.

particularly beneficial in applications where energy absorption, impact resistance, and flexibility are paramount, such as in cushioning systems or biomedical implants.

2.2. Gradient TPMS porous structures

To obtain a gradient TPMS porous structure with varying density along a single direction, the linear gradient implicit surface design method is employed. This method derives linear equations for the design parameters (*T*) of the Primitive (P) and Gyroid (G) TPMS porous structures along the Z-axis, where T represents parameters such as porosity or material density. The method ensures a continuous variation in density, facilitating the fabrication of gradient structures with controlled material properties. This relationship is expressed by the following equation:

$$T_{P(G)} = \mathrm{K} \cdot \mathrm{Z} + T_0 \tag{4}$$

Where k and T_0 can be determined using the values from the top and bottom points (Z_{min}, $T\rho^* = 0.3$) and (Z_{max}, $T\rho^* = 0.5$), respectively, to establish a linear gradient with relative densities ranging from 30% to 50%.

The structural gradient design of porous structures involves a smooth transition of joining two or more porous structures. Mathematical definitions of gradual polymorphism transitions are possible during the structural gradient process. The weighting function enables the assignment of various TPMS topologies to specific regions within hybrid porous structures, ensuring seamless transitions between them. Inspired by an effective and concise method, this can be achieved using [36]:

$$\varphi_{hyb} = \mu(x, y, z) \cdot \varphi_P + \left[1 - \mu(x, y, z) \cdot \varphi_G\right] \tag{5}$$

Where φ_{hyb} is the structural gradient porous structures composed of φ_P and φ_G, and $\mu(x,y,z)$ is a spatial weighting function describing the monotonic function using [37]:

$$\mu(\mathrm{x}, \mathrm{y}, \mathrm{z}) = \frac{1}{1 + e^{kf(x,y,z)}} \tag{6}$$

Where, $\mu(x, y, z) \in [0,1]$, k determines the transformation width. $f(x, y, z)$ denotes the spatial coordinates that define the form transformations in different regions. Boundary $f(x, y, z)$ marks the transformation boundary of the structural gradient TPMS porous structure. To achieve structural gradient porous structures influences in the direction of the z-axis (loading direction), we stipulate $f(x, y, z) = -z$. Figure 2 plots the S-shaped function following a single orientation utilizing several values. Hybrid TPMS designs, such as those combining Primitive

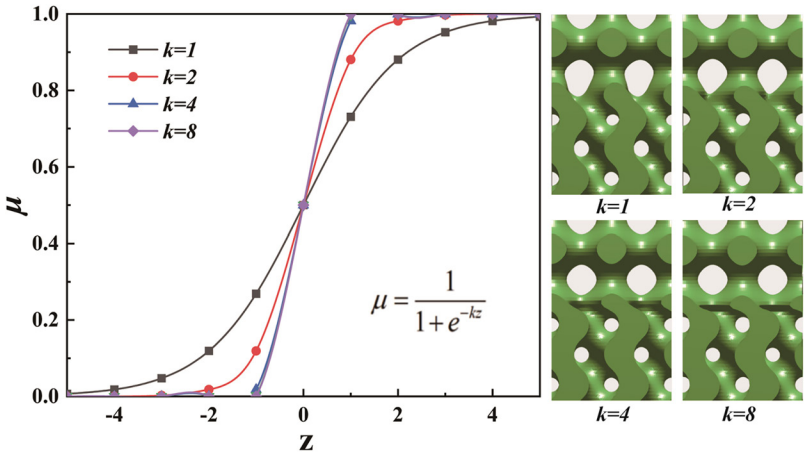

Figure 2: Sigmoid function and Primitive-Gyroid porous structure with different *k* values.

Table 1: Design information of TPMS porous structures.

	UNIFORM		DENSITY GRADIENT		STRUCTURAL GRADIENT
Unit	P	G	P	G	P&G
Porosity	30,40,50	30,40,50	30–50	30–50	40
Cell size, mm^3	4				
Cells, mm	8 × 8 × 8				
Dimension, m^3	32 × 32 × 32				

and Gyroid topologies, have shown enhanced mechanical performance. WANG *et al.* reported improved yield strength and energy absorption in such hybrid systems [38].

Different TPMS porous structures can be obtained using the above methods. In all cases, the domain x∈[32, 32], y∈[32, 32], z∈[32, 32] is defined to obtain the samples with a 32 × 32 × 32 mm specimen in Magcis 22.0 software. The specific parameters of the uniform, density gradient, and structural gradient samples are listed in Table 1. Figure 3 shows the models for uniform Primitive (U-P), uniform Gyroid (U-G), density

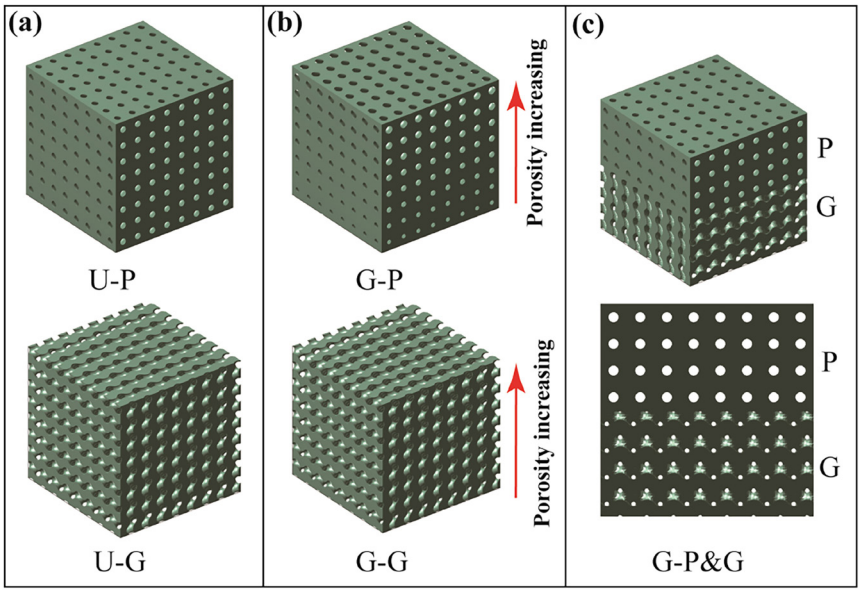

Figure 3: Designed models of TPMS structures: (a) Uniform; (b) Density gradient; (c) Structural gradient.

gradient Primitive (G-P), density gradient Gyroid (G-G), and structural gradient Primitive and Gyroid (G-P&G) structures.

2.3. Additive manufacturing

The specimens were fabricated using Bamboo P1P equipment developed by Shenzhen Bambu Lab Co. The PLA filament used in this study is purchased from Shenzhen Bambu Lab Co (PLA Basic), with mechanical specifications provided by the manufacturer as follows: tensile strength of 35 ± 4 MPa, elastic modulus of 2.75 ± 0.16 GPa, and elongation at break of 12.2 ± 1.8%. The fused deposition modeling (FDM) printing parameters used in this work are: 220 °C printing temperature, 0.2 mm layer thickness, 105 mm/s outer layer molding speed, 200 mm/s filling speed, and other parameters were kept constant. The material was a filament with a diameter dimension of 1.75 ± 0.03 mm. To achieve higher print quality, the material was baked in an oven at 55 °C for eight hours. Three specimens were fabricated using the same manufacturing process described above.

2.4. Characterization

Structural characterization was performed using a GP-660V optical microscope and an EVO-18 scanning electron microscope (SEM, Carl Zeiss AG) to assess the molding accuracy of the TPMS specimens. The internal structure was also scanned using a micro-computed tomography scanner (CT, Nanotom, Phoenix Contact), which provides detailed spatial and contrast resolution. The scanning parameters were as follows: 120 kV voltage,100 μA current, and a 0.2 °rotation step. After scanning, the 3D computed tomography (CT) images were imported into VGStudi for analysis. The mass of the specimens was determined using an electronic balance (HJT-C, Huajie). The porosity was calculated separately using the weighing method:

$$\rho^* = \frac{m_1}{m_2} \times 100\% \tag{7}$$

Where m_1 represents the physical weight of the manufactured porous structure, m_2 stands for the physical weight of the solid structure with an equivalent volume.

2.5. Quasi-static experimental testing

Based on ASTM D1621-2010, uniaxial compressive experiments were conducted using a mechanical testing machine (UTM6104, Shanghai Sansi Machinery Manufacturing Co., Ltd, Shanghai, China) with a load capacity of 10 kN to evaluate the mechanical properties. Compression tests were conducted on three specimens of each structure at a loading rate of 2 mm/min. As exhibited in Figure 4, the specimens were positioned at the center of a round plate, where only the overhead plate was permitted to shift downward to apply compression. The lateral expansion of the samples was unrestricted during compression. No lubricant was applied between the specimen and compression platens. The unconstrained lateral expansion of specimens during testing intentionally simulated realistic friction conditions between the material and rigid surfaces in practical applications. A minimal preload of 5 N (<0.1% of the ultimate load) was applied prior to testing to ensure full contact between the

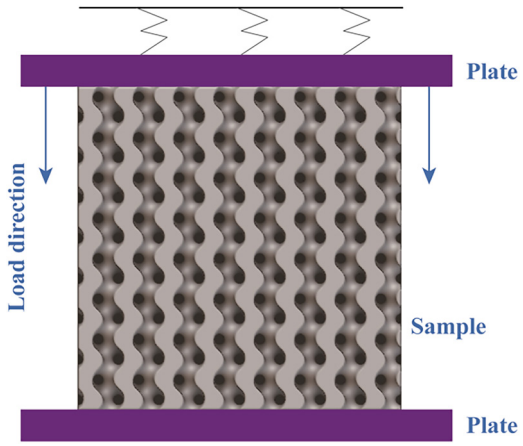

Figure 4: Schematic diagram of compressive test.

specimen and platens while avoiding pre-deformation. The entire compression process was documented through video recording. Proper accounting for toe regions in the stress-strain calculations is essential. In this analysis, toe regions were excluded from the stress-strain curve data to minimize any potential inaccuracies caused by non-uniform stress distribution at the edges of the specimen. The analysis focused on the central region of the specimen, where the compressive load was uniformly applied. Following the tests, stress-strain curve data for the specimens were analyzed, and key performance indicators were extracted from these curves.

3. RESULTS AND DISCUSSION

3.1. Manufacturing accuracy and morphological analysis

The theoretical and measured porosities of the samples were compared, as displayed in Table 2 and Figure 5, respectively. The results show that the actual porosity is slightly lower than the intended, with deviations of 1.27% to 3.82%. This indicates high manufacturing accuracy using FDM. For uniform porous structures, the deviation between the fabricated and theoretical porosity steadily decreased with increasing porosity. This deviation is caused by tiny particles, agglomerated particles, and cured raw materials adhering to the edges of the aperture.

The samples fabricated using fused deposition modeling (FDM) are presented in Figure 6. The results indicate that each structure retained its integrity after processing. The pore characteristics, including uniform

Table 2: Theoretical and measured porosities of samples.

SAMPLE	THEORETICAL POROSITY(%)	MEASURED POROSITY(%)	DEVIATION(%)
U-P-30	30	28.82 ± 0.11	3.93 ± 0.36
U-P-40	40	39.11 ± 0.13	2.23 ± 0.32
U-P-50	50	49.08 ± 0.09	1.84 ± 0.18
U-G-30	30	28.73 ± 0.18	4.23 ± 0.60
U-G-40	40	38.85 ± 0.16	2.87 ± 0.40
U-G-50	50	48.71 ± 0.11	2.58 ± 0.22
G-P-40	40	39.02 ± 0.14	2.45 ± 0.35
G-G-40	40	38.89 ± 0.08	2.77 ± 0.20
G-P&G-40	40	39.00 ± 0.10	2.51 ± 0.25

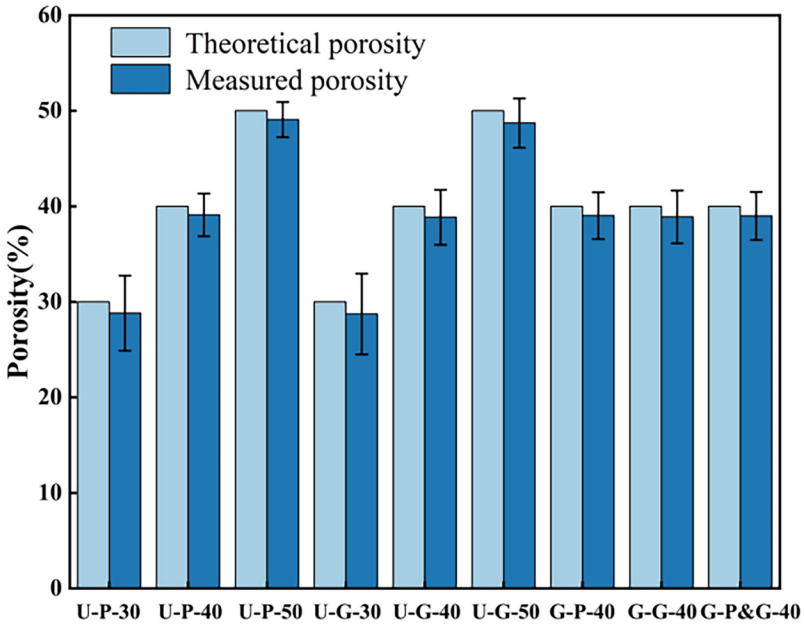

Figure 5: Comparison between theoretical and measured porosities of samples.

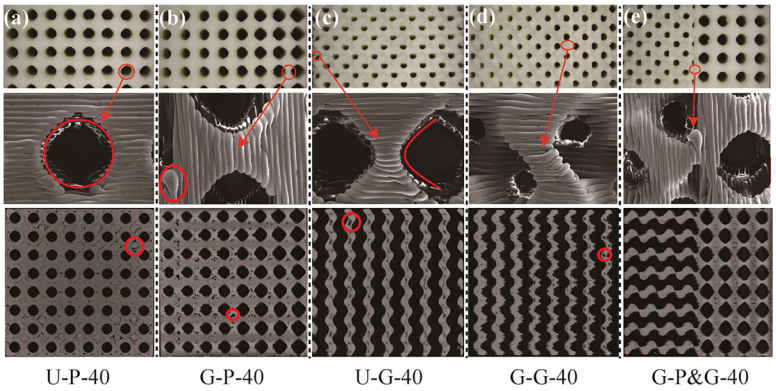

Figure 6: Images of the fabricated samples: (a) U-P-40; (b) G-P-40; (c) U-G-40; (d) G-G-40 and (e) G-P&G-40.

and gradient porosity, align with the intended design specifications. The two-dimensional (2D) slice images of the G and P porous structures, characterized by micro-CT, are shown in Figure 6. It can be observed that the CT images exhibit excellent interconnectivity and gradient porosity in the porous structures along the design direction. Moreover, the density gradient structure shows a continuous increase in porosity, with a well-defined gradient distribution in accordance with the design specifications. For the gradient structures, the structural integrity at the transition remained intact, confirming the feasibility of the design approach. For the uniform porous structures, deviations in pore geometry increased with rising porosity, likely due to limitations in printing precision. Micro-pores and internal defects were observed in most of the samples, affecting the connectivity of the pore network. These variations are due to the inherent limitations of the 3D printing process, including layer misalignment and surface irregularities. Although SEM imaging would offer additional surface detail, micro-CT was used to capture both internal and external morphology of the TPMS lattices with a voxel size of 10 μm. The CT reconstructions confirm that the printed strut surfaces and pore geometries closely reproduce the intended CAD features (deviations≤3.93%). Future work will include SEM characterization to further validate FDM surface fidelity. This study used FDM-printed PLA to explore TPMS design principles. Although process-induced deviations occurred, they align with typical FDM tolerances [36]. Future work will verify these trends using metal SLM and multi-material printing to decouple geometry-driven effects from process-specific artifacts.

3.2. Compression properties and deformation behaviour

3.2.1. Deformation

The stress-strain curves of uniform and gradient porous structures, shown in Figure 5, illustrate the mechanical behavior under compression. The deformation process consists of three key stages as outlined by SALEH *et al.* [39]. In the linear elastic stage, an increase in porosity from 30% to 50% leads to a decrease in the slope of the curves, indicating a reduction in the elastic modulus. This increase also extends the plateau region, which is characterized by a relatively constant stress level. This phenomenon occurs due to the reduction in the thickness of the porous structure as porosity increases, leading to a decrease in overall compressive strength and stiffness. As strain increases, porous structures with lower porosity transitioned into the densification phase earlier, characterized by a steady increase in stress. This phenomenon is attributed to the increased wall thickness and smaller pore size, which limit the available volume for material densification. Similar observations regarding the relationship between porosity and mechanical performance have been reported in previous studies [40, 41], further supporting the findings of this study.

The distinction lies in the behavior of uniform and density-gradient Primitive porous structures, which exhibit fluctuations during the plateau stress phase. This behavior indicates a progressive failure of individual layers throughout the compressive process. The curves of the P structures show a repeating pattern of fluctuations, suggesting that one layer after another was crushed during compression [42]. The curves of the U-P-30, U-P-40, and G-P-40 structures show fluctuations at the plateau stress stage, indicating that the deformation mechanism is similar for all three structures, as depicted in Figure 7(a). The U-P-30, U-P-40, and G-P-40 structures reached the densification stage in sequence, with increasing porosity leading to earlier densification, as shown in Figure 5(a). Figure 6 shows that the first layer collapses at approximately 0.15 strain for the U-P-50 samples, a phenomenon also observed in Figure 7(a). This behavior is attributed to the high pore density of the U-P-50

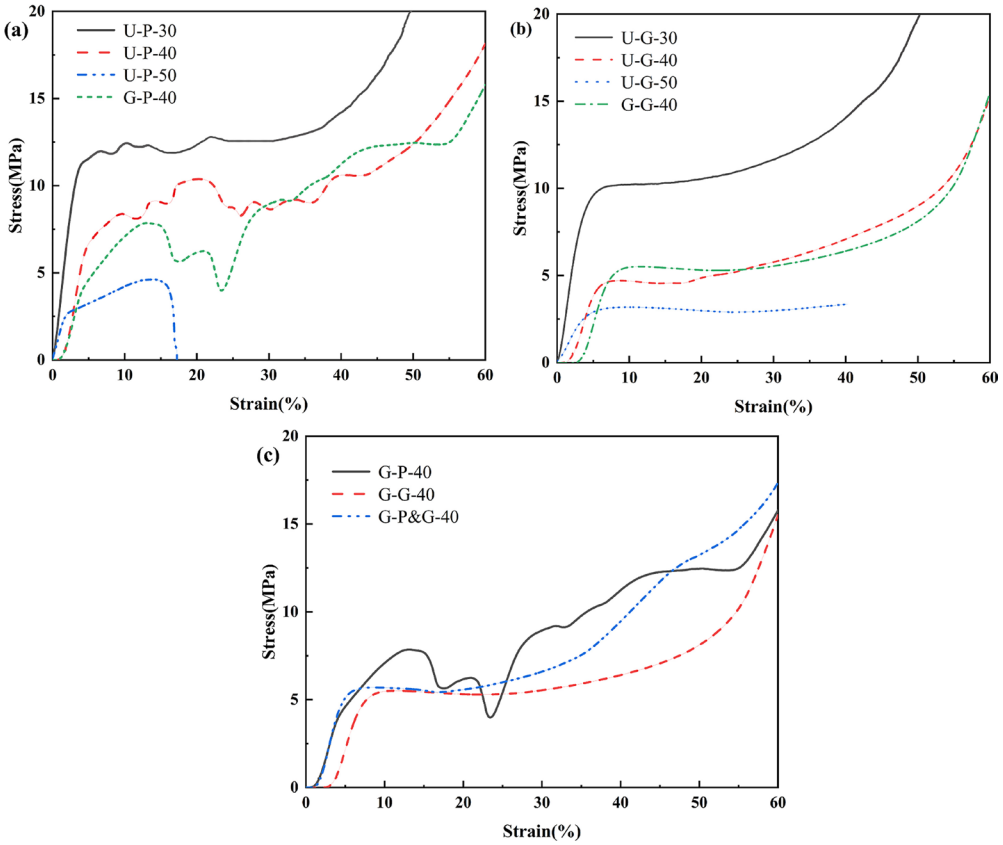

Figure 7: Stress-strain curves of uniform and gradient porous structures: (a) Primitive; (b) Gyroid; c) Primitive and Gyroid.

structure and the overall buckling triggered by the collapse of the first layer during compression. Figure 5(c) compares the curves of the structural gradient G&P samples with the density gradient G-P and G-G samples, all having the same porosity. At low strain levels, the G-G porous structures exhibited behavior comparable to that of the G-P porous structures. At higher strain levels, the G-G porous structure reduced the magnitude of fluctuations in the plateau stress phase observed in the G-P structures and increased the yield strength of the G-G structure. Various technical applications, such as impact and ballistic protection, can benefit from this behavior, particularly due to the improved mechanical performance under high strain conditions.

As illustrated in Figure 8, the uniform and density gradient G porous structures primarily exhibited shear failure. The deformation predominantly occurred along the specimen's diagonal direction, which is in agreement

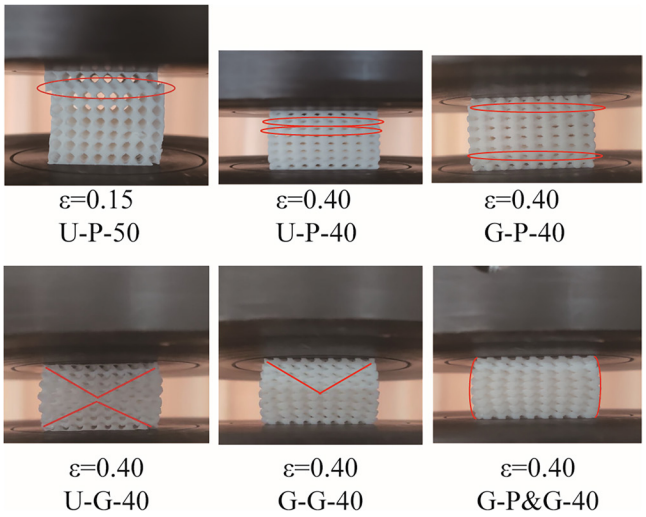

Figure 8: Compressive deformation of uniform and gradient porous structures.

with the findings of [43], where similar shear failure modes were observed. In contrast to the P structure, the G structure mainly displays a 'V'-shaped deformation pattern, differing from the layer-by-layer sequential deformation seen in the P structure. Figure 8 shows that the U-P structure forms 'X'-shaped shear bands, while the U-G structure develops 'V'-shaped shear bands at a strain of 0.4. Notably, the G-P&G specimens exhibited a characteristic drum-shaped shear band pattern. Although SEM fracture surface analysis was not performed in this study, our observations are consistent with common failure modes observed in TPMS lattices, where the high-porosity regions initiate failure. Future work will include SEM analysis to directly observe the fracture surfaces and confirm the post-failure mechanisms.

3.2.2. Mechanical properties

The yield strength and elastic modulus of TPMS porous structures are shown in Figure 9. Figure 9(a) shows that the yield strengths of U-P structures are 11.26 MPa and 2.24 MPa at porosities of 30% and 50%, respectively. Figure 9(b) shows that the elastic modulus decreases from 309.8 MPa to 167.1 MPa. Consequently, the yield strength and elastic modulus of P structures declined as porosity increased. Similarly, Figures 9(a) and 9(b) show that the yield strength and elastic modulus of uniform G structures decreased as porosity rose from 30% to 50%. These findings align with experimental results reported by other researchers [40]. This decrease in mechanical performance is attributed to the larger pore sizes and thinner walls caused by the higher porosity.

The Figures 9(a) and 9(b) show that the yield strength of U-P-40 (8.56 MPa) is higher than that of G-P-40 (7.78 MPa) by 10.03% despite having the same porosity. This outcome occurred because the G-P-40 sample initially failed in the top layer, which had lower porosity compared to the U-P-40 sample. The elastic modulus of U-P-40 (243.7 MPa) was higher than that of G-P-40 (151.9 MPa). This result can be attributed to the greater load capacity resulting from the increased cell thickness of the P structure. However, the yield strength of U-G-40 (4.48 MPa) is lower than that of G-G-40 (5.27 MPa) by 14.99% with the same porosity. The elastic modulus of G-G-40 (140.7 MPa) is greater than U-G-40 (135.9 MPa). The results indicate that the mechanical properties of porous structures are affected by variations in pore density and the specific design of the cell structure.

The Gibson-Ashby theory provides a framework for establishing the connection amid yield strength, elastic modulus, and relative density, a method commonly employed in prior research [44]. The Gibson-Ashby predictive model is represented by the following mathematical equations:

$$E^* = \frac{E}{E_s} = C_E \left(\frac{\rho}{\rho_s} \right)^{n_E} = C_E (1 - \rho^*)^{n_E} \tag{8}$$

$$\sigma^* = \frac{\sigma}{\sigma_s} = C_\sigma \left(\frac{\rho}{\rho_s} \right)^{n_\sigma} = C_\sigma (1 - \rho^*)^{n_\sigma} \tag{9}$$

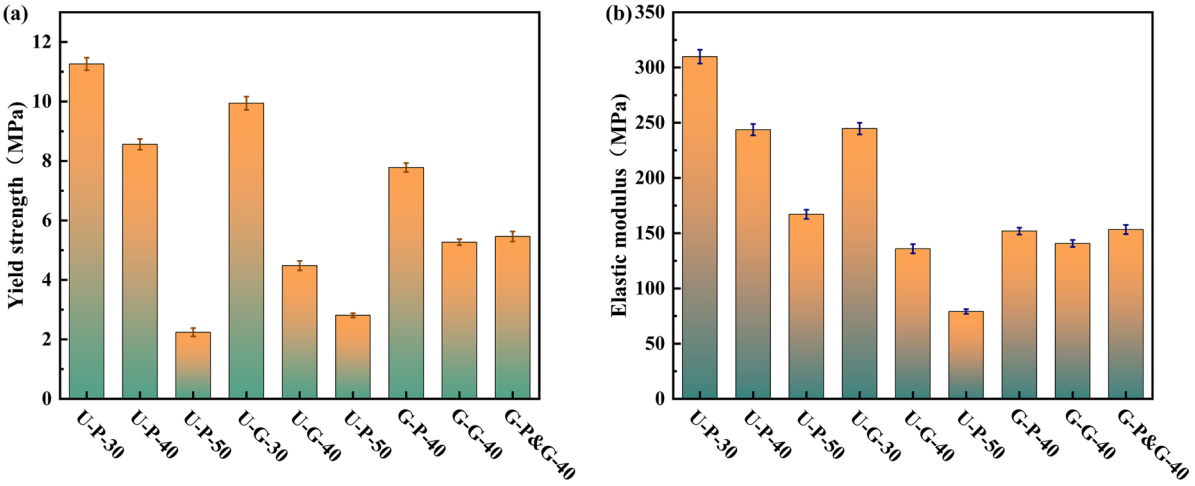

Figure 9: Mechanical properties of uniform and gradient porous structures: (a) Yield strength; (b) Elastic modulus.

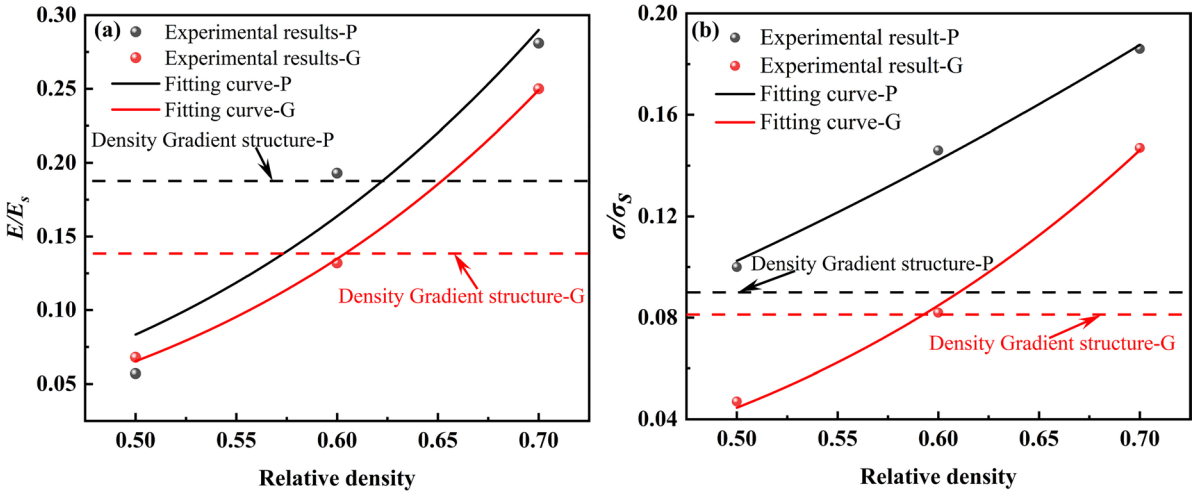

Figure 10: Gibson-Ashby patterns fitted for TPMS structures: (a) compressive modulus and (b) yield strength as a function of the relative density.

Where E is the elastic modulus. σ represents yield strength. ρ* stands for porosity of TPMS porous structure. E_s corresponds solid samples' elastic modulus. σ_s denotes yield strength. ρ_s stands for density. E/E_s serves as the relative elastic modulus. σ/σ_s denotes relative yield strength. ρ/ρ_s stands for relative density. c_E and c_σ represent the design variables. n_E and n_σ stand for scaling factors of which the values are associated with the lattice arrangement. The relationships among relative yield strength (σ*), relative elastic modulus (E*) and relative density were determined, as illustrated in Figure 10.

The results indicate that E/E_s and σ/σ_s for the various porous structures increase as porosity decreases. The P structures exhibited better mechanical characteristics than the G structures as evidenced by the E/E_s and σ/σ_s curves, which were greater at the same porosity. The difference in σ/σ_s between the P and G structures with minimal at 50% porosity but gradually increased with rising relative density.

3.3. Energy absorption performance

TPMS porous structures are widely utilized in energy absorption applications, where their performance is determined by the sum of energy absorbed in each unit volume. Furthermore, the energy absorbed from the initial loading point up to the onset of the densification phase can be calculated as described in prior studies [45].

$$W_\varepsilon = \int_0^\varepsilon \sigma(\varepsilon) d\varepsilon \tag{10}$$

Where W_ε denotes the total energy absorption per unit volume, σ(ε) represents the stress corresponding to strain ε, and ε represents the strain.

The strain cutoff at 0.4 was chosen as it corresponds to the onset of densification for most TPMS structures, where energy absorption is most effective. While extending the cutoff to 0.6 or densification onset would likely increase the total absorbed energy, this would primarily reflect the material's resistance to compression rather than effective energy dissipation. Future studies will investigate energy absorption over a wider strain range to capture the full energy dissipation behavior, including the densification phase. The results for strains up to 0.4 are outlined in Table 3. As illustrated in Figure 11, energy absorption efficiency improves with increasing porosity, but the overall energy absorption capacity is also influenced by the timing of the deformation phases. For structures with lower porosity, the linear elastic deformation phase and the densification phase occur earlier in the loading process, which limits their total energy absorption capacity. In contrast, higher porosity TPMS structures can deform more extensively before densification begins, allowing them to absorb a greater amount of energy. This characteristic is particularly beneficial for applications where extended energy dissipation is critical, such as in crash barriers or protective packaging.

The energy absorption of each unit volume in the U-P-30 structure was 5.46 J/mm^3, whereas that of the U-G-30 was 4.18 J/mm^3. The two structures demonstrated higher elastic energy absorption per unit volume

Table 3: Energy absorption of the samples.

PROPERTIES	U-P-30	U-P-40	U-P-50	U-G-30	U-G-40	U-G-50	G-P-40	G-G-40	G-P&G-40
Wε(J/mm^3)	5.46	3.29	–	4.18	1.90	1.15	2.71	1.91	2.30

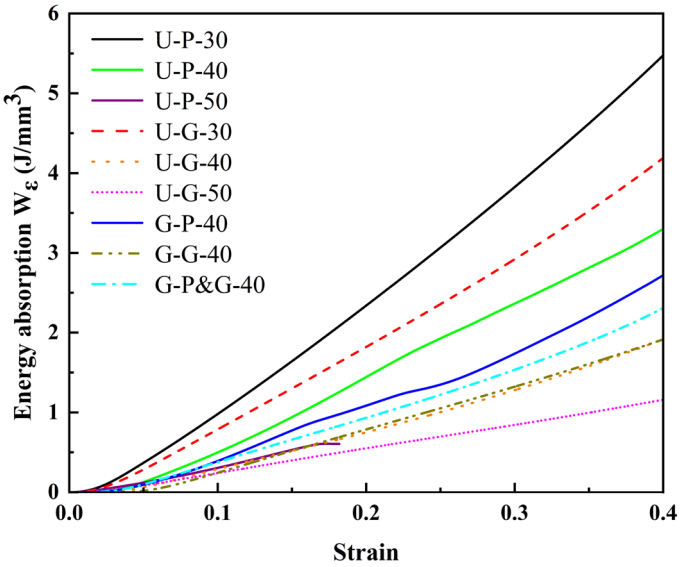

Figure 11: Energy absorption per unit volume versus strain curves of porous structures.

compared to other TPMS structures. In addition, the energy absorption efficiencies of G-P-40, G-G-40, and G-P&G-40 with the same porosity are measured as 2.71, 1.91, and 2.30, respectively. The unit cell type used in the TPMS structure also has a significant impact on energy absorption performance. For instance, the U-P-30 and U-P-40 generally demonstrated higher energy absorption per unit volume compared to U-G-30 and G-P-40, despite having similar porosities. This can be attributed to the differing geometrical and mechanical behaviors of the unit cells. The Primitive unit cell, with its more compact and structurally supportive geometry, allows for more efficient deformation under compressive forces, leading to a greater ability to absorb energy before failure. This comparison highlights the importance of cell design selection to achieve the desired energy absorption characteristics. TPMS structures with gradient porosity exhibited significantly higher energy absorption efficiency compared to uniform TPMS structures with the same porosity. The gradual transition in porosity across these gradient structures allows for more controlled deformation under compressive loading. This results in a more effective distribution of stress and a higher overall energy absorption capacity, particularly in dynamic or impact scenarios. The ability to design structures with a continuous change in porosity provides a versatile solution for applications where high energy dissipation is required without compromising the structural integrity of the material. The U-P-50 sample exhibited premature failure under compression at lower strains due to excessive deformation in the low-density regions, preventing us from reaching the 0.4 strain cutoff for energy absorption calculations. As such, the energy absorption value for this condition is not available.

As illustrated in Figure 11, energy absorption efficiency improves with increasing porosity, but the overall energy absorption capacity is also influenced by the timing of the deformation phases. For structures with lower porosity, the linear elastic deformation phase and the densification phase occur earlier in the loading process, which limits their total energy absorption capacity. In contrast, higher porosity TPMS structures can deform more extensively before densification begins, allowing them to absorb a greater amount of energy. This characteristic is particularly beneficial for applications where extended energy dissipation is critical, such as in crash barriers or protective packaging.

4. CONCLUSIONS

This study investigated the mechanical properties, deformation behavior, and energy absorption performance of uniform, gradient, and structural gradient TPMS porous structures, fabricated using fused deposition modeling (FDM). The following key conclusions were drawn from the results:

(1) The measured porosities of the uniform porous structures were slightly lower than the designed values, with deviations ranging from 1.27% to 3.82%. This suggests that the FDM process provides a high level of manufacturing precision, with deviations well within acceptable limits for typical 3D printing applications.

(2) Uniform and gradient porous structures exhibited distinct deformation behaviors under compression. Increasing porosity resulted in a decrease in yield strength and elastic modulus, with the Primitive (P) structures consistently outperforming the Gyroid (G) structures at the same porosity levels in terms of mechanical strength. The gradient TPMS structures demonstrated superior mechanical performance, particularly in the G-P and G-G configurations, where variations in material density contributed to enhanced mechanical properties.

(3) The deformation process of the porous structures under compression was characterized by three key stages: the linear elastic phase, plateau stress phase, and densification phase. The P structures showed a more gradual transition between these phases, while the G structures exhibited a more abrupt shift. The gradient structures, particularly those with a G-P configuration, displayed improved mechanical performance under high strain conditions, which is beneficial for impact and ballistic protection applications.

(4) Increasing the porosity of the structures resulted in enhanced energy absorption capabilities, as more void space is available for energy dissipation. Notably, the P structures exhibited higher energy absorption compared to the G structures at the same porosity. Additionally, the gradient G structures demonstrated an even higher energy absorption capacity than their uniform counterparts, emphasizing the potential of gradient designs for applications requiring high energy dissipation.

5. ACKNOWLEDGMENTS

The author would like to acknowledge the financial support from Anhui Province Scientific Research Planning Foundation (2022AH051911 and 2024AH051163).

6. BIBLIOGRAPHY

[1] MA, S., TANG, Q., FENG, Q., *et al.*, "Mechanical behaviours and mass transport properties of bone-mimicking scaffolds consisted of Gyroid structures manufactured using selective laser melting", *Journal of the Mechanical Behavior of Biomedical Materials*, v. 93, pp. 158–169, 2019. doi: http://doi.org/10.1016/j.jmbbm.2019.01.023. PubMed PMID: 30798182.

[2] AL-SAEDI, D.S.J., MASOOD, S.H., FAIZAN-UR-RAB, M., *et al.*, "Mechanical properties and energy absorption capability of functionally graded F2BCC lattice fabricated by SLM", *Materials & Design*, v. 144, pp. 32–44, 2018. doi: http://doi.org/10.1016/j.matdes.2018.01.059.

[3] YANG, L., MERTENS, R., FERRUCCI, M., *et al.*, "Continuous graded Gyroid cellular structures fabricated by selective laser melting: Design, manufacturing and mechanical properties", *Materials & Design*, v. 162, pp. 394–404, 2019. doi: http://doi.org/10.1016/j.matdes.2018.12.007.

[4] ZHAO, L., PEI, X., JIANG, L., *et al.*, "Bionic design and 3D printing of porous titanium alloy scaffolds for bone tissue repair", *Composites. Part B, Engineering*, v. 162, pp. 154–161, 2019. doi: http://doi.org/10.1016/j.compositesb.2018.10.094.

[5] FENG, Y., GUO, X., HUANG, K., *et al.*, "Enhanced electromagnetic microwave absorption of SiOC ceramics targeting the integration of structure and function", *Journal of the European Ceramic Society*, v. 41, n. 13, pp. 6393–6405, 2021. doi: http://doi.org/10.1016/j.jeurceramsoc.2021.06.007.

[6] GADO, M.G., AL-KETAN, O., AZIZ, M., *et al.*, "Triply periodic minimal surface structures: design, fabrication, 3D printing techniques, state-of-the-art studies, and prospective thermal applications for efficient energy utilization", *Energy Technology*, v. 12, n. 5, pp. 2301287, 2024. doi: http://doi.org/10.1002/ente.202301287.

[7] THAI, C.H., HUNG, P.T., NGUYEN-XUAN, C., *et al.*, "A meshfree method for functionally graded triply periodic minimal surface plates", *Composite Structures*, v. 332, pp. 117913, 2024. doi: http://doi.org/10.1016/j.compstruc.2025.107660.

[8] PHUNG-VAN, P., HUNG, P.T., THAI, H., *et al.*, "Small-dependent nonlinear analysis of functionally graded triply periodic minimal surface nanoplates using nonlocal strain gradient theory", *Composite Structures*, v. 335, pp. 117986, 2024. doi: http://doi.org/10.1016/j.compstruct.2024.117986.

[9] ZHANG, Z., PAN, E., ZHOU, J., *et al.*, "Indentation over a transversely isotropic, poroelastic, and layered half-space", *Applied Mathematical Modelling*, v. 127, pp. 439–453, 2024. doi: http://doi.org/10.1016/j.apm.2023.12.027.

[10] LESMANA, L.A., LU, C., CHEN, F., *et al.*, "Triply periodic minimal surface gyroid structure as effective metal hydride hydrogen storage reactor: experimental study", *Thermal Science and Engineering Progress*, v. 42, pp. 101903, 2023. doi: http://doi.org/10.1016/j.tsep.2023.101903.

[11] KARAMI, K., BLOK, A., WEBER, L., *et al.*, "Continuous and pulsed selective laser melting of Ti6Al4V lattice structures: effect of post-processing on microstructural anisotropy and fatigue behaviour", *Additive Manufacturing*, v. 36, pp. 101433, 2020. doi: http://doi.org/10.1016/j.addma.2020.101433.

[12] TAN, L.J., ZHU, W., SAGAR, K., *et al.*, "Comparative study on the selective laser sintering of polypropylene homopolymer and copolymer: processability, crystallization kinetics, crystal phases and mechanical properties", *Additive Manufacturing*, v. 37, pp. 101610, 2021. doi: http://doi.org/10.1016/j.addma.2020.101610.

[13] SALEH, M., ANWAR, S., AL-AHMARI, A.M., *et al.*, "Prediction of mechanical properties for carbon fiber/PLA composite lattice structures using mathematical and ANFIS models", *Polymers*, v. 15, n. 7, pp. 1720, 2023. doi: http://doi.org/10.3390/polym15071720. PubMed PMID: 37050334.

[14] ALIZADEH-OSGOUEI, M., LI, Y., VAHID, A., *et al.*, "High strength porous PLA Gyroid scaffolds manufactured via fused deposition modeling for tissue-engineering applications", *Smart Materials in Medicine*, v. 2, pp. 15–25, 2024. doi: http://doi.org/10.1016/j.smaim.2020.10.003.

[15] ZHAO, M., LIU, F., ZHANG, Y., *et al.*, "Impact of PLA modifications on mechanical properties and degradation behavior for biomedical performance", *European Polymer Journal*, v. 131, pp. 106–116, 2020. doi: http://doi.org/10.1515/epoly-2020-0046.

[16] LI, X., WANG, C., ZHANG, Y., "PLA composites and their potential for industrial applications in manufacturing porous structures with enhanced properties", *Journal of Materials Processing Technology*, v. 281, pp. 116952, 2020. doi: http://doi.org/10.1016/j.jmatprotec.2020.116952.

[17] YE, H., TIAN, F., HE, W., *et al.*, "Mechanical and thermal property analysis and optimization design of hybrid lattice structure based on triply periodic minimal surfaces", *Thin-walled Structures*, v. 203, pp. 112203, 2024. doi: http://doi.org/10.1016/j.tws.2024.112203.

[18] AL-KETAN, O., ROWSHAN, R., PALAZOTTO, A.N., *et al.*, "On mechanical properties of cellular steel solids with shell-like periodic architectures fabricated by selective laser sintering", *Journal of Engineering Materials and Technology*, v. 141, n. 2, pp. 021009, Apr. 2019. doi: http://doi.org/10.1115/1.4041874.

[19] LI, H., YANG, W., MA, Q., *et al.*, "Specific sensitivity analysis and imitative full stress method for optimal BCCZ lattice structure by additive manufacturing", *Crystals*, v. 12, n. 12, pp. 1844, 2022. doi: http://doi.org/10.3390/cryst12121844.

[20] PARK, K.M., MIN, K.S., ROH, Y.S., "Design optimization of lattice structures under compression: study of unit cell types and cell arrangements", *Materials*, v. 15, n. 1, pp. 97, 2021. doi: http://doi.org/10.3390/ma15010097. PubMed PMID: 35009238.

[21] AL-OMARI, S.A.B., QASEM, M., *et al.*, "Design and performance assessment of a triply-periodic-minimal-surface structures-enhanced gallium heat sink for high heat flux dissipation: a numerical study", *Applied Thermal Engineering*, v. 257, 2024. doi: http://doi.org/10.1016/j.applthermaleng.2024.124154.

[22] GADO, M.G., "Improving the charging performance of latent heat thermal energy storage systems using triply periodic minimal surface (TPMS) structures", *Journal of Energy Storage*, v. 103, pp. 114310, 2024. doi: http://doi.org/10.1016/j.est.2024.114310.

[23] GIBSON, L.J., ASHBY, M.F., *Cellular solids: structure and properties*, 2 ed., Cambridge, Cambridge University Press, 1997. doi: http://doi.org/10.1017/CBO9781139878326.

[24] AL-KETAN, O., LEE, D.W., AL-RUB, R.K.A., "Mechanical properties of additively-manufactured sheet-based gyroidal stochastic cellular materials", *Additive Manufacturing*, v. 48, pp. 102418, 2021. doi: http://doi.org/10.1016/j.addma.2021.102418.

[25] JIA, H., LEI, H., WANG, P., *et al.*, "An experimental and numerical investigation of compressive response of designed Schwarz Primitive triply periodic minimal surface with non-uniform shell thickness", *Extreme Mechanics Letters*, v. 37, pp. 100671, 2020. doi: http://doi.org/10.1016/j.eml.2020.100671.

[26] AL-KETAN, O., LEE, D.W., ROWSHAN, R., *et al.*, "Functionally graded and multi-morphology sheet TPMS lattices: Design, manufacturing, and mechanical properties", *Journal of the Mechanical Behavior*

of Biomedical Materials, v. 102, pp. 103520, 2020. doi: http://doi.org/10.1016/j.jmbbm.2019.103520. PubMed PMID: 31877523.

[27] LIANG, Y., ZHOU, W., LIU, Y., *et al.*, "Energy absorption and deformation behavior of 3D printed triply periodic minimal surface stainless steel cellular structures under compression", *Steel Research International*, v. 92, n. 3, pp. 2000411, 2020. doi: http://doi.org/10.1002/srin.202000411.

[28] PENG, C., FOX, K., QIAN, M., *et al.*, "3D printed sandwich beams with bioinspired cores: mechanical performance and modelling", *Thin-walled Structures*, v. 161, pp. 107471, 2021. doi: http://doi.org/10.1016/j.tws.2021.107471.

[29] CAO, X., YANG, H., REN, X., *et al.*, "Mechanical performance and defect analysis of the imperfect micro smooth gyroid cylinder shell structure", *Composite Structures*, v. 273, pp. 114320, 2021. doi: http://doi.org/10.1016/j.compstruct.2021.114320.

[30] PENG, C., TRAN, P., MOURITZ, A.P., "Compression and buckling analysis of 3D printed carbon fibre-reinforced polymer cellular composite structures", *Composite Structures*, v. 300, pp. 116167, 2022. doi: http://doi.org/10.1016/j.compstruct.2022.116167.

[31] HU, W., CAO, X., ZHANG, X., *et al.*, "Deformation mechanisms and mechanical performances of architected mechanical metamaterials with Gyroid topologies: synchrotron X-ray radiation in-situ compression experiments and 3D image based finite element analysis", *Extreme Mechanics Letters*, v. 44, pp. 101229, 2021. doi: http://doi.org/10.1016/j.eml.2021.101229.

[32] LU, C., ZHANG, Y., AZIZ, M., *et al.*, "Mechanical behaviors of multidimensional gradient gyroid structures under static and dynamic loading: a numerical and experimental study", *Additive Manufacturing*, v. 59, pp. 103187, 2022. doi: http://doi.org/10.1016/j.addma.2022.103187.

[33] HIRMUKHE, S.S., PRASAD, K.E., SINGH, I., "Finite element analysis of deformation and failure mechanisms in nanoscale hexagonal cellular structures of metallic glasses", *Mechanics of Materials*, v. 160, pp. 103946, 2021. doi: http://doi.org/10.1016/j.mechmat.2021.103946.

[34] YOO, D.J., "Computer-aided porous scaffold design for tissue engineering using triply periodic minimal surfaces", *International Journal of Precision Engineering and Manufacturing*, v. 12, n. 1, pp. 61–71, 2011. doi: http://doi.org/10.1007/s12541-011-0008-9.

[35] SREEDHAR, N., THOMAS, N., AL-KETAN, O., *et al.*, "Mass transfer analysis of ultrafiltration using spacers based on triply periodic minimal surfaces: effects of spacer design, directionality and voidage", *Journal of Membrane Science*, v. 561, pp. 89–98, 2018. doi: http://doi.org/10.1016/j.memsci.2018.05.028.

[36] ALIZADEH-OSGOUEI, M., LI, Y., VAHID, A., *et al.*, "High strength porous PLA gyroid scaffolds manufactured via fused deposition modeling for tissue-engineering applications", *Smart Materials in Medicine*, v. 2, pp. 15–25, 2021. doi: http://doi.org/10.1016/j.smaim.2020.10.003.

[37] ZHANG, J., XIE, S., LI, T., *et al.*, "A study of multi-stage energy absorption characteristics of hybrid sheet TPMS lattices", *Thin-walled Structures*, v. 190, pp. 110989, 2023. doi: http://doi.org/10.1016/j.tws.2023.110989.

[38] WANG, C., YAN, S., LI, Y., *et al.*, "Improved mechanical behavior of hybrid structures designed with triply periodic minimal surfaces", *Materials Today. Communications*, v. 46, pp. 112581, 2025. doi: http://doi.org/10.1016/j.mtcomm.2025.112581.

[39] SALEH, M., ANWAR, S., AL-AHMARI, A., *et al.*, "Compression performance and failure analysis of 3D-Printed carbon fiber/PLA composite TPMS lattice structures", *Polymers*, v. 14, n. 21, pp. 4595, 2022. doi: http://doi.org/10.3390/polym14214595. PubMed PMID: 36365590.

[40] ČAPEK, J., MACHOVÁ, M., FOUSOVÁ, M., *et al.*, "Highly porous, low elastic modulus 316L stainless steel scaffold prepared by selective laser melting", *Materials Science and Engineering*, v. 69, pp. 631–639, 2016. doi: http://doi.org/10.1016/j.msec.2016.07.027. PubMed PMID: 27612756.

[41] ZHANG, C., ZHENG, H., YANG, L., *et al.*, "Mechanical responses of sheet-based Gyroid-type triply periodic minimal surface lattice structures fabricated using selective laser melting", *Materials & Design*, v. 214, pp. 110407, 2022. doi: http://doi.org/10.1016/j.matdes.2022.110407.

[42] SALEH, M., ANWAR, S., AL-AHMARI, A., *et al.*, "Compression performance and failure analysis of 3D-printed carbon fiber/PLA composite TPMS lattice structures", *Polymers*, v. 14, n. 21, pp. 4595, 2022. doi: http://doi.org/10.3390/polym14214595. PubMed PMID: 36365590.

[43] NOVAK, N., AL-KETAN, O., KRSTULOVIĆ-OPARA, L., *et al.*, "Quasi-static and dynamic compressive behaviour of sheet TPMS cellular structures", *Composite Structures*, v. 266, pp. 113801, 2021. doi: http://doi.org/10.1016/j.compstruct.2021.113801.

[44] FAN, X., TANG, Q., FENG, Q., *et al.*, "Design, mechanical properties and energy absorption capability of graded-thickness triply periodic minimal surface structures fabricated by selective laser melting", *International Journal of Mechanical Sciences*, v. 204, pp. 106586, 2021. doi: http://doi.org/10.1016/j.ijmecsci.2021.106586.

[45] LI, S., LIU, Z., SHIM, V.P.W., *et al.*, "In-plane compression of 3D-printed self-similar hierarchical honeycombs – Static and dynamic analysis", *Thin-walled Structures*, v. 157, pp. 106990, 2020. doi: http://doi.org/10.1016/j.tws.2020.106990.